



Effects of Stabilization Heat Treatment on Microstructure and Mechanical Properties of Si-Bearing 15Cr–9Ni–Nb Austenitic Stainless Steel Weld Metal

Yakui Chen^{1,2} · Dong Wu¹ · Dianzhong Li¹ · Yiyi Li^{1,3} · Shanping Lu^{1,3}

Received: 26 July 2022 / Revised: 5 September 2022 / Accepted: 18 September 2022 / Published online: 8 December 2022
© The Chinese Society for Metals (CSM) and Springer-Verlag GmbH Germany, part of Springer Nature 2022

Abstract

Two 15Cr–9Ni–Nb austenitic stainless steel weld metals with 2.5% Si and 3.5% Si (namely 2.5Si and 3.5Si samples, respectively) were designed and prepared through tungsten inert gas (TIG) welding and then hold at 800 °C or 900 °C for 3 h for stabilization. The microstructure and mechanical properties were investigated both for the as-welded and after-stabilization heat treatment (SHT) weld metals. There are 3.0–4.0% martensite and 2.5–3.5% δ ferrite in the 2.5Si as-welded weld metal and 6.0–7.0% δ ferrite in the 3.5Si as-welded weld metal. After SHT, a large amount of martensite formed in the 2.5Si weld metal, and $\delta \rightarrow \gamma$ transition occurred during the SHT process both for the 2.5Si and 3.5Si weld metals. There were a large amount of coarse NbC and few nanoscale NbC in the as-welded weld metal. During the SHT, a large amount of nanoscale NbC formed in the matrix, while a large number of G phases formed at the austenite grain boundaries and the δ/γ interfaces. The decrease in solid solution C and δ ferrite content led to the decline of the yield strength of the weld metal after SHT. The martensite formed in 2.5Si weld metal after SHT had less effect on strength because of its low carbon content. The G phases formed during the SHT reduced the impact energy of the weld metal because it promoted the intergranular fracture, while the $\delta \rightarrow \gamma$ transition reduced the amount of the δ/γ interfaces and avoided the intergranular fracture, which was beneficial for the impact toughness of the weld metals.

Keywords Austenitic stainless steel · Weld metal · Stabilization heat treatment · Martensite · NbC · $\delta \rightarrow \gamma$ transition

1 Introduction

Austenitic stainless steel is widely used in nuclear reactors as the cladding and pressure vessel materials for its excellent creep failure resistance and stability at high temperatures [1]. Lead fast reactor (LFR), one of the Gen-IV reactors, also

uses austenitic stainless steel as popular candidate materials, such as AISI 316 and modified 316 steel [1–4]. The LFR uses liquid lead or lead–bismuth eutectic (LBE) as a coolant. The corrosion resistance of the austenitic stainless steels to liquid lead and LBE is challenged by its high Ni content due to the high solubility of Ni in the liquid lead and LBE [5, 6]. The 15Cr–9Ni–Nb (EP302) austenitic stainless steel used in Russia was developed with a lower Ni content and higher Si content compared with the common austenitic stainless steel [7], which improved the resistance to lead–bismuth eutectic corrosion.

Generally, the alloy design of austenitic stainless steel should comply with the principle of δ ferrite as the initial phase of solidification to avoid solidification cracks [8]. For the weld metal, most of the δ ferrite formed during solidification is transformed to austenite during the cooling of the weld metal, while a small amount of δ ferrite exists in the weld metal. The residual δ ferrite is metastable and will transform to $M_{23}C_6$, σ phase, and χ phase during high-temperature service; these will degrade the mechanical

Available online at <http://link.springer.com/journal/40195>.

✉ Shanping Lu
shplu@imr.ac.cn

¹ Shenyang National Laboratory for Materials Science, Institute of Metal Research, Chinese Academy of Sciences, Shenyang 110016, China

² School of Materials Science and Engineering, University of Science and Technology of China, Shenyang 110016, China

³ CAS Key Laboratory of Nuclear Materials and Safety Assessment, Institute of Metal Research, Chinese Academy of Sciences, Shenyang 110016, China

properties of the weld metal [9–13]. The content of the residual δ ferrite is controlled by the Ni equivalent and Cr equivalent of the weld metal. As a ferritizing element, the increase in Si addition increases the Cr equivalent, which ultimately affects the content of δ ferrite in the weld metal. Because the contents of Cr and Ni in the 15Cr–9Ni–Nb steel are lower than the common austenitic stainless steel, the austenitic stability of 15Cr–9Ni–Nb austenitic stainless steel will also be reduced [14]. The martensite transformation temperature will rise, and trace changes in elements may have a significant effect on the microstructure of the 15Cr–9Ni–Nb steel weld metal.

Because of the high-temperature service environment (350–650 °C) [15], Nb is added to the 15Cr–9Ni–Nb steel for the stabilization of C atoms during a stabilization heat treatment (SHT) where the NbC carbide will form. The temperature of the SHT is required to be higher than the sensitization temperature to avoid the formation of $M_{23}C_6$ carbide. The austenite in 15Cr–9Ni–Nb steel is metastable at room temperature [14], and the effect of C reduction in the matrix during the SHT on the microstructure and mechanical properties of the weld metal is worth investigating in detail. In addition, precipitation during SHT can also have an impact on the mechanical properties of the weld metal [16, 17]. But, there are few reports on the microstructure and

mechanical properties of 15Cr–9Ni–Nb austenitic stainless steel or weld metal.

In this work, two 15Cr–9Ni–Nb steel weld metals with different Si contents were designed and prepared. The microstructure characteristics and mechanical properties were investigated both for the as-welded and after-SHT weld metals. The effect of SHT on the phase transformation and precipitation behavior and mechanical properties was discussed. The work aims to provide fundamental data on the welding materials design for 15Cr–9Ni–Nb steel, which could facilitate the application of 15Cr–9Ni–Nb steel on LFR.

2 Experimental

2.1 Weld metal Preparation and Heat Treatment

The diameter of the filler wire is 1.2 mm, and the wire is numbered as 2.5Si and 3.5Si according to the Si content. The chemical composition of the filler wire is shown in Table 1. The weldment design is shown in Fig. 1a, the size of the base metal is 350 mm × 150 mm × 20 mm, and the size of the backing plate is 350 mm × 20 mm × 10 mm. Tungsten inert gas (TIG) welding was used to prepare the weld metal;

Table 1 Chemical composition of filler wire and weld metal (wt%)

Element	C	Si	Mn	Cr	Ni	Nb
2.5Si filler wire	0.057	2.45	1.64	14.03	8.28	0.73
2.5Si weld metal	0.059	2.49	1.44	14.07	8.47	0.71
3.5Si filler wire	0.064	3.37	1.63	13.92	8.31	0.72
3.5Si weld metal	0.065	3.43	1.45	13.96	8.38	0.70

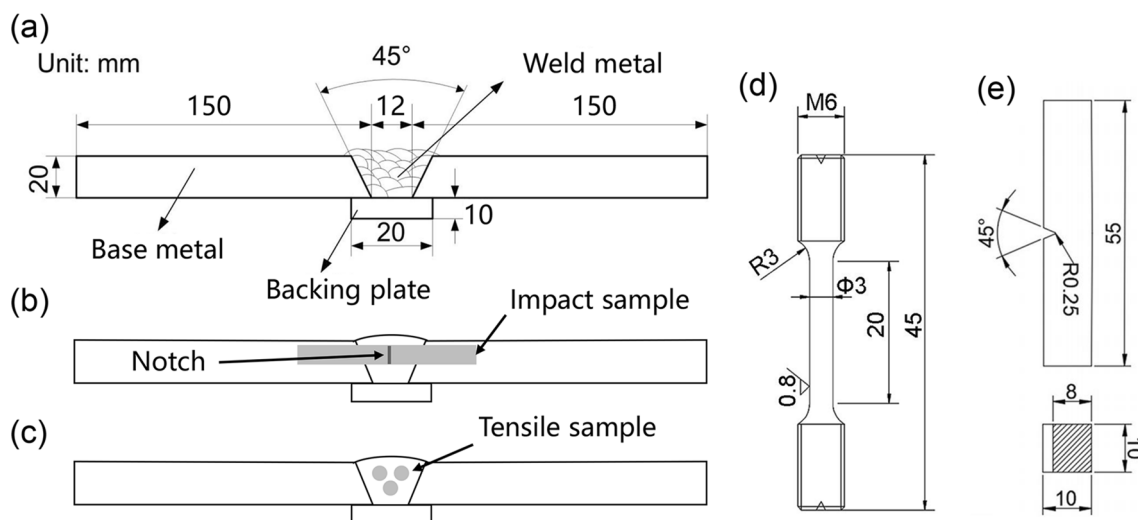


Fig. 1 Schematic diagram of **a** weldment, location of **b** the impact sample and **c** the tensile sample in the weld metal, the dimensions of **d** the tensile sample and **e** the impact sample

Table 2 Welding parameters

Welding current	Welding voltage	Welding speed	Wire feed speed	Shield gas	Gas flow rate	Interpass temperature
180–182 A	13–13.5 V	0.1 m/min	1 m/min	99.999% Argon	15 L/min	< 100 °C

the welding parameters are listed in Table 2. The chemical composition of the weld metal is listed in Table 1.

The SHT after welding was carried out at 800 °C/3 h or 900 °C/3 h and then furnace-cooled to room temperature. The weld metals after SHT were numbered as 2.5Si-800, 3.5Si-800, 2.5Si-900, and 3.5Si-900.

2.2 Mechanical Properties Tests

The KB-30-SA Vickers hardness machine was used to measure the microhardness of the weld metal with a load of 100 g. For Charpy V-notch impact test, samples were cut along the transverse direction of the weld metal, with the notch machined in the cross section of the weld metal. The location of the impact samples is shown in Fig. 1b, and the dimensions of the impact samples are shown in Fig. 1e. A SANS-ZBC2452-C machine was operated at room temperature to evaluate the impact toughness. Standard cylindrical tensile samples were cut from the lengthwise direction of the weld metal, as shown in Fig. 1c, and the sample specification is shown in Fig. 1d. Tensile tests were conducted at room temperature in the INSTRON-5982 machine equipped with an extensometer, which could automatically record the deformation until fracture, and the elongation was then calculated. In each condition of the weld metal, three tensile samples and three impact samples were tested, respectively. After testing, the fracture characteristic was examined by scanning electron microscopy (SEM) to analyze the fracture mode.

2.3 Microstructure Characterization

Microstructure specimens were cut from the cross-section of the weld metal, ground, and finally polished by 2.5 μm diamond paste. After the 90 s of erosion by a solution of 1 g picric acid + 5 ml hydrochloric acid + 100 ml alcohol, an optical microscope (OM) was used to observe microstructure, and SEM equipped with energy-dispersive spectroscopy (EDS) was utilized the phase and precipitation. A transmission electron microscope (TEM; Talos F200X) was also used to observe and identify the phase and precipitation.

The electrochemical extraction of the precipitates in the as-welded and after-SHT weld metals was conducted in the solution of 10% hydrochloric acid and 90% methanol solution at room temperature under the constant extraction current of 0.2 A. The residue was rinsed, dried, and collected. The precipitation types and contents of the residue were analyzed by X-ray diffraction (XRD) analysis equipment with a $\text{CuK}\alpha$ source.

3 Result and Discussion

3.1 Thermodynamic Calculation

The Thermo-Calc with TCFE 8 database was employed to predict the phase and precipitations possibly formed in the weld metal. The result is shown in Fig. 2. According to the calculation results, the solidification mode of the weld metals was FA mode (ferrite–austenite mode) [8], i.e., primary ferrite precipitation followed on further cooling, with

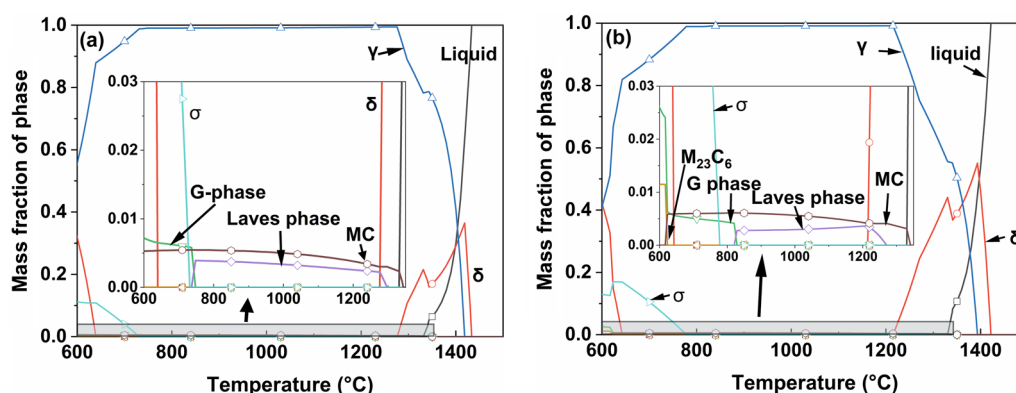


Fig. 2 Calculated result by Thermo-Calc: **a** 2.5Si, **b** 3.5Si. (γ =austenite, δ = δ ferrite, σ = σ phase)

austenite formation in the three-phase region, which was a eutectic reaction. The elevated content of Si could increase the Cr equivalent and raise the content of δ ferrite during solidification (shown in Fig. 2), as a result increasing the content of δ ferrite in the weld metal at room temperature. In the 2.5Si and 3.5Si weld metal, MC -type carbides started to ($M = Nb$ in this work) precipitate at a temperature of about 1330 °C and reached their maximum amount near 800 °C. Except for MC , laves phase and G phase precipitated in both weld metals. The precipitation start temperature of laves phase in 2.5Si, and 3.5Si was 1290 and 1260 °C, and the precipitation starts temperature of the G phase in 2.5Si and 3.5Si weld metal was 740 and 830 °C. The precipitation start temperature of $M_{23}C_6$ in 3.5Si weld metal was 620 °C and below 600 °C in 2.5Si weld metal. The formation temperature of σ phase in both 2.5Si and 3.5Si weld metal was below 800 °C.

The purpose of SHT is to precipitate MC and avoid the formation of $M_{23}C_6$. Therefore, based on the calculation results, the SHT temperature should be higher than 800 °C.

3.2 Phase Transition

3.2.1 Microstructure of As-Welded Weld Metals

The metallographic photograph (Fig. 3a, d) shows the presence of martensite in the 2.5Si as-welded weld metal. The FN (ferrite number) (as listed in Table 3) was obtained by ferritometer measurement and represents the content of magnetic phases, i.e., BCC phases, including δ ferrite and martensite in the weld metal. The δ ferrite content in the as-welded weld metal was obtained from metallographic statistics, and the phase contents of the 2.5Si and 3.5Si as-welded

Table 3 Phase contents of the as-welded weld metals

Weld metal	FN	Phase content
2.5Si	6.5	2.5%–3.5% δ ferrite + 3.0%–4.0% Martensite + Balanced Austenite
3.5Si	6.4	6.0%–7.0% δ ferrite + Balanced Austenite

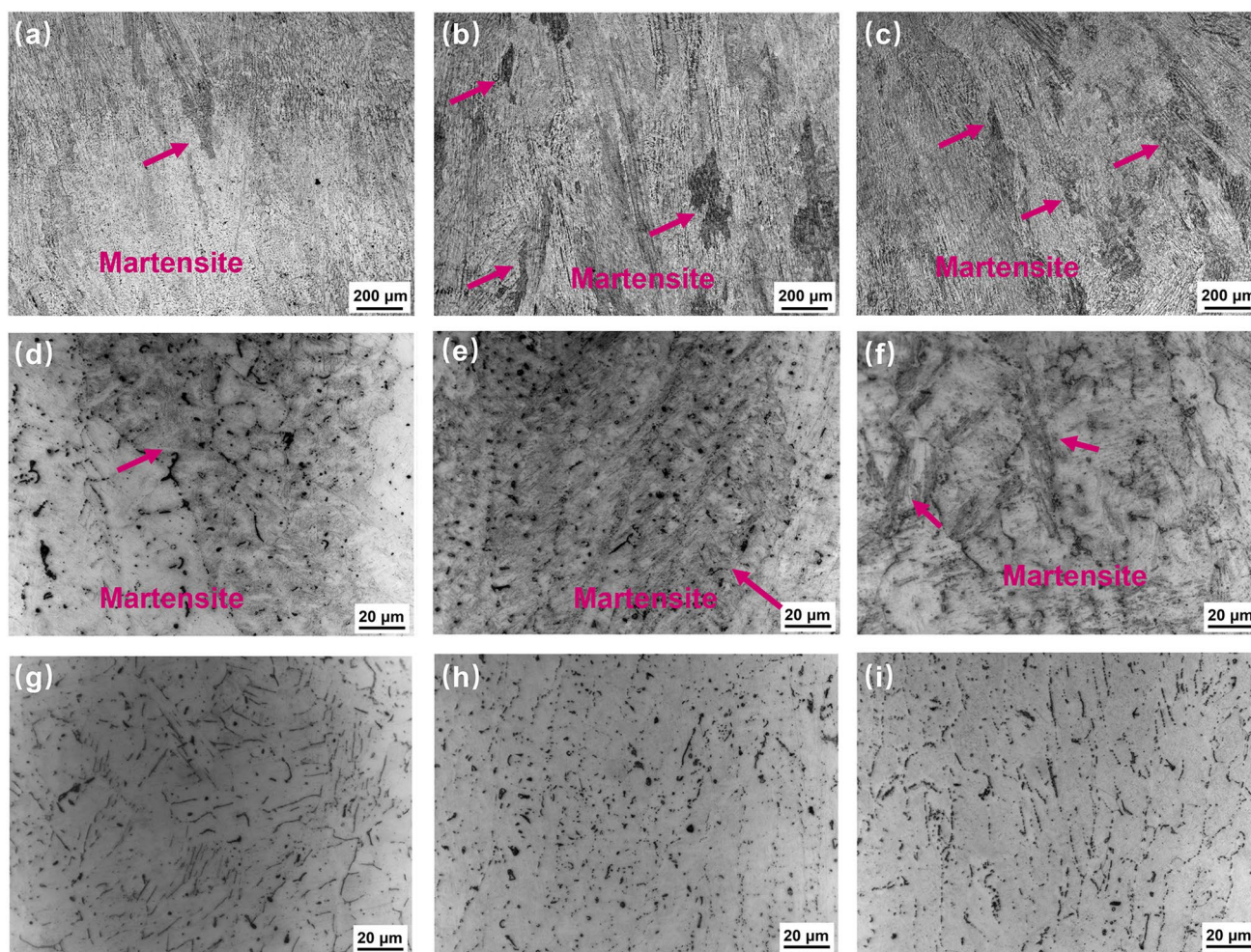


Fig. 3 OM images of the weld metals: **a, d** 2.5Si, **b, e** 2.5Si-800, **c, f** 2.5Si-900, **g** 3.5Si, **h** 3.5Si-800, **i** 3.5Si-900

weld metals are listed in Table 3. Due to the lower Ni content, 15Cr–9Ni–Nb steel weld metal has fragile austenitic stability, which results in 3.0%–4.0% martensite in the 2.5Si as-welded weld metal. In addition, there is 2.5%–3.5% δ ferrite in 2.5Si as-welded weld metal, and the rest are austenite. With the increase in Si content, the martensite transformation temperature was lowered [18], and no martensite formed in the 3.5Si as-welded weld metal, as shown in Fig. 3g. The δ ferrite content is 6.0%–7.0% in the 3.5Si as-welded weld metal, which is consistent with the result of ferritometer measurement.

3.2.2 Martensite Transition

The FNs of the weld metals after SHT are shown in Fig. 4. The FNs of 2.5Si, 2.5Si-800, and 2.5Si-900 samples are 6.5, 37.2, and 38.9, respectively, indicating that the FNs of 2.5Si significantly increased after SHT. The significant increase in FNs in 2.5Si samples after SHT is due to the formation of a large amount of martensite in the weld metal, as shown in Fig. 3b, c, e, and f. The SEM and TEM image and the corresponding selected-area electron diffraction (SAED) pattern of the martensite in 2.5Si-900 weld metal are shown

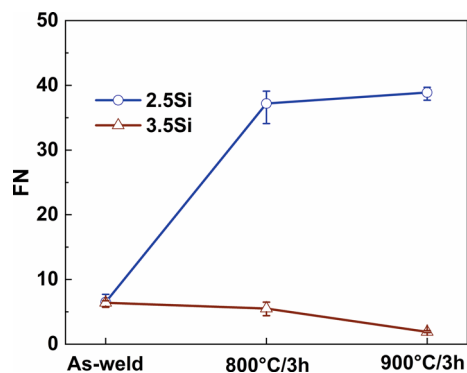


Fig. 4 FNs of the as-welded and after-SHT weld metals

in Fig. 5. The formation of martensite was caused by the reduction of free C in the matrix. The 2.5Si as-welded weld metal already had very fragile austenite stability, the solid solution of C atoms in the matrix was reduced through MC phase precipitation during the SHT process, and the austenite stability was further reduced, so more martensite transition occurred during the cooling to room temperature.

3.2.3 $\delta \rightarrow \gamma$ Transition

The FNs of 3.5Si, 3.5Si-800, and 3.5Si-900 samples are 6.4, 5.5, and 1.9, respectively, indicating a decreasing trend after SHT. No martensite was observed in 3.5Si weld metal after SHT (as shown in Fig. 3h, i). Figure 6 shows the characterization of δ ferrite in 3.5Si as-welded and after-SHT weld metals. Compared to the δ ferrite in the 3.5 Si as-welded weld metal (as shown in Fig. 6a), a small portion of the original large ferrite has been transformed into austenite in the 3.5Si-800 weld metal (as shown in Fig. 6b), and the γ_δ (austenite transitioned by δ ferrite during the SHT) area becomes larger in the 3.5Si-900 weld metal (as shown in Fig. 6c). The evolution of δ ferrite in the as-welded and after-SHT weld metals is consistent with the change of FNs in the 3.5Si weld metal. The $\delta \rightarrow \gamma$ transition during SHT is the reason for the decreasing FN, and the content of the $\delta \rightarrow \gamma$ transition after 900 °C/3 h is more than that of 800 °C/3 h. The high-magnification TEM image of 3.5Si-900 is shown in Fig. 6d. It can be seen that the original large piece of δ ferrite has been mostly transformed into austenite, and the δ/γ interface has disappeared, leaving the precipitations originally located at the interfaces.

The $\delta \rightarrow \gamma$ transition during heat treatment has been observed in some studies [19]. The diffusion of elements across the δ/γ interfaces controlled the $\delta \rightarrow \gamma$ transition [20]. During cooling after solidification, δ ferrite was continuously transformed into austenite, accompanied by austenitizing elements such as Ni, C, Mn, etc. diffusing into ferrite, while ferritizing elements such as Cr, Nb, Si, etc. were

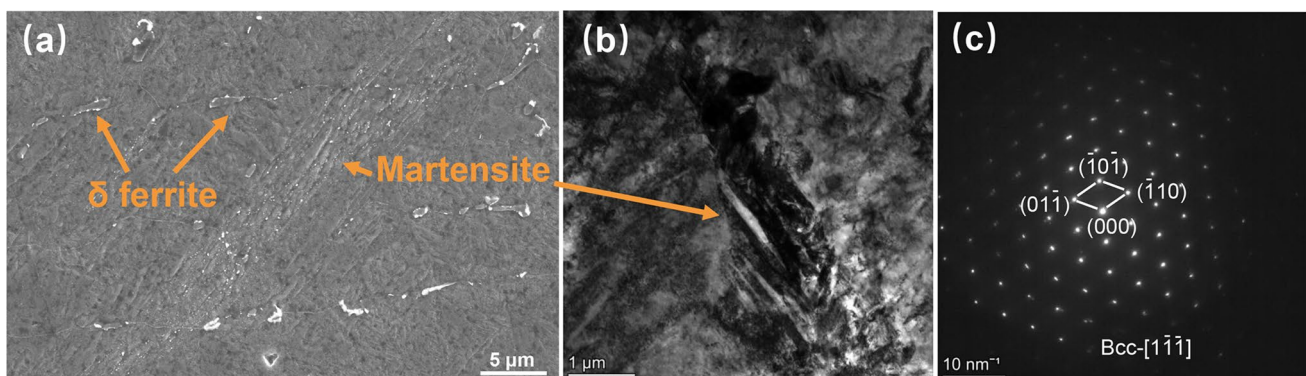


Fig. 5 a SEM and b TEM images, c corresponding SAED pattern of Martensite in 2.5Si-900 weld metal

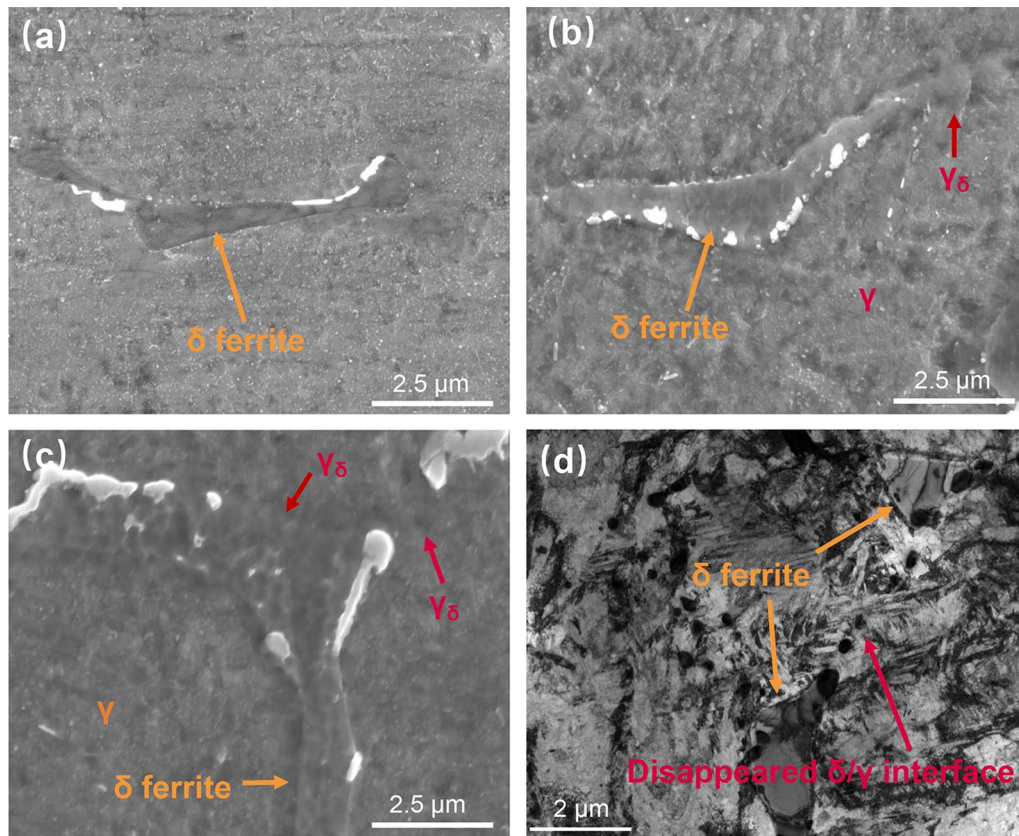


Fig. 6 Characterization of δ ferrite: SEM image of **a** 3.5Si as-welded weld metal and **b** 3.5Si-800 weld metal, **c** 3.5Si-900 weld metal, TEM image of **d** 3.5Si-900 weld metal (γ_δ =austenite transitioned by δ ferrite during the SHT)

enriched in δ ferrite. This process stopped only when the diffusion of elements was restricted at some lower temperature. The residual δ ferrite was enriched in ferritizing elements and depleted in austenitizing elements [8]. During the SHT, the elements could continue to diffuse while the $\delta \rightarrow \gamma$ transition occurred. Since the element's diffusion rate was affected by temperature, the SHT temperature affected the amount of $\delta \rightarrow \gamma$ transition. In the 3.5Si weld metal, FN decreased more after 900 °C/3 h treatment than 800 °C/3 h because the element had a higher diffusion rate at 900 °C, resulting in more $\delta \rightarrow \gamma$ transition. The 2.5Si weld metal also had $\delta \rightarrow \gamma$ transition during the SHT, although the amount of transition is difficult to be determined by the FN variation due to the influence of the martensite.

3.3 Precipitation

3.3.1 Precipitation Behavior in the As-Welded Weld Metal

The results of the analysis of the precipitations species in the weld metal by XRD are shown in Fig. 7. In both 2.5Si and 3.5Si as-welded weld metals, the only precipitation is NbC (as shown in Fig. 7a). Generally, in stabilized austenitic

stainless steel, there are two types of MC, one is primary particles generally formed during solidification with large size in 1–10 μm range, and the other is secondary precipitation with small size in 5–500 nm range [21–23]. Generally, MC carbides precipitation is predominantly intragranular, on dislocations and stackings faults, but MC precipitation at grain boundaries can also occur [24–26]. In this work, it was found that there are also two kinds of NbC, the coarse one and the nanoscale one. As shown in Figs. 8 and 9, the coarse-NbC with size among 1 μm , which is primary particles, is distributed in the matrix and at the δ/γ interfaces. The maps of elements distribution of the coarse-NbC in the matrix are shown in Fig. 8b, c, and d. The EDS semiquantitative results of the coarse-NbC at the δ/γ interfaces, the δ ferrite, and the matrix are shown in Fig. 9b–d, and Table 4. As shown in Fig. 10a, there are only a few nanoscale NbC distributed in the matrix because of the fast cooling rate after solidification. The size of nanoscale NbC is mainly 5–20 nm.

3.3.2 Precipitation Behavior during SHT

As shown in Fig. 10b, the number of dispersed nanoscale-NbC increased significantly in the 3.5Si weld metal after

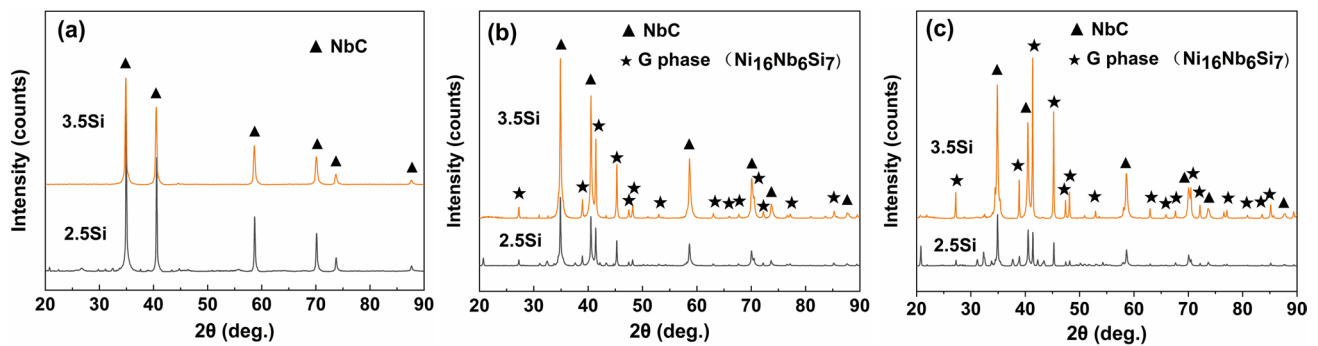


Fig. 7 XRD analysis results of precipitations in weld metal: **a** as-welded, **b** 800 °C/3 h, **c** 900 °C/3 h

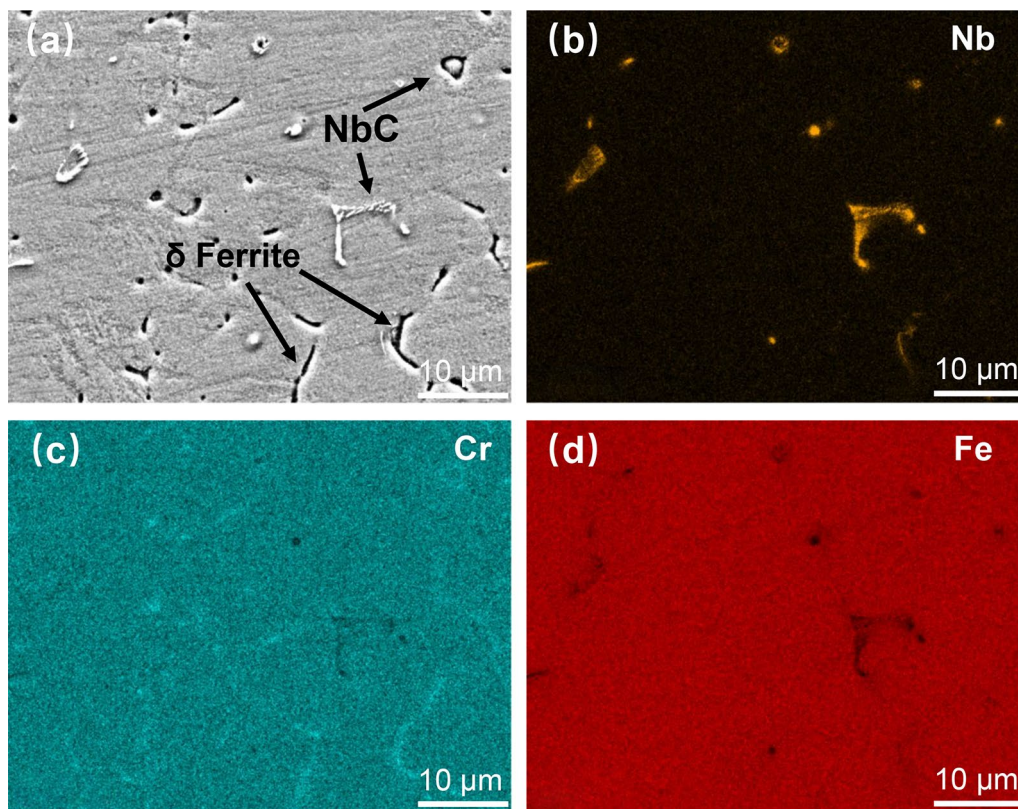


Fig. 8 Microstructure characterization of the coarse-NbC in the matrix of the 2.5Si as-welded weld metal: **a** SEM image of NbC and δ ferrite, elements distribution of **b** Nb, **c** Cr, and **d** Fe

SHT, which means that a large amount of nanoscale NbC precipitated in the matrix during SHT. Compared to the precipitation behavior after welding, the NbC formed during the SHT was mainly nanoscale species due to the precipitation temperature. The size of nanoscale NbC is also mainly concentrated in the range of 5–20 nm. However, the increase in the densities of NbC with a size of 5–10 nm in the 3.5Si-900 weld metal is more significant than the densities of NbC with a size of 10–20 nm, as shown in Fig. 10.

According to the XRD results (as shown in Fig. 7b, c), after SHT, the G phases were precipitated in both 2.5Si and 3.5Si weld metals at either 800 °C/3 h or 900 °C/3 h. With the increasing Si content, both the number and the intensity of diffraction peaks of G phases rise, which indicated that the number of G phases in the 3.5Si weld metal after SHT is more than those in 2.5Si weld metal after SHT. The transmission characterization of the G phase is shown in Fig. 11. The chemical composition of the G phase was determined as $\text{Ni}_{16}\text{Nb}_6\text{Si}_7$ based on the diffraction pattern and scanning

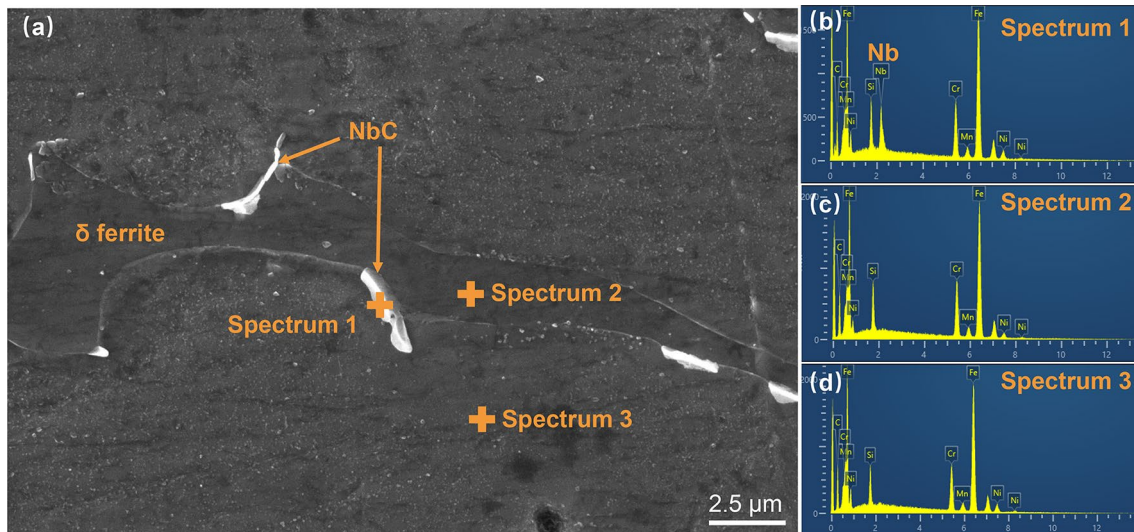


Fig. 9 Microstructure characterization of the coarse-NbC at the δ/γ interfaces of the 3.5Si as-welded weld metal: **a** SEM image, EDS semiquantitative result of **b** spectrum 1 (NbC), **c** spectrum 2 (δ ferrite), **d** spectrum 3 (austenite)

Table 4 EDS semiquantitative result in Fig. 9

Element	Spectrum 1		Spectrum 2		Spectrum 3	
	wt%	at.%	wt%	at.%	wt%	at.%
C	9.44	32.44	12.00	37.68	12.83	39.69
Si	2.86	4.21	3.39	4.55	2.87	3.80
Cr	12.91	10.25	15.23	11.05	12.79	9.14
Mn	1.43	1.08	1.36	0.93	1.23	0.83
Fe	60.87	44.97	63.90	43.15	63.45	42.22
Ni	5.86	4.12	4.12	2.65	6.83	4.32
Nb	6.62	2.94	—	—	—	—
Total	100	100	100	100	100	100

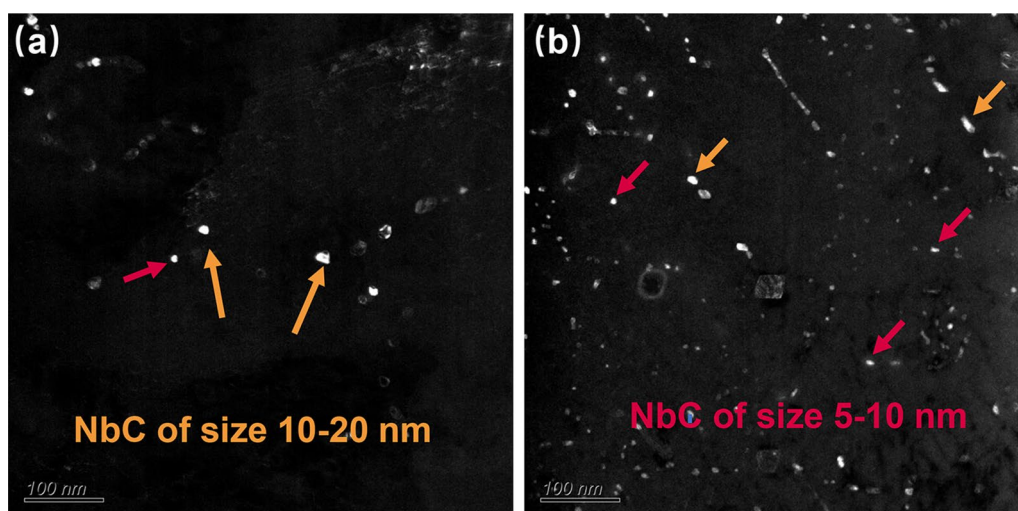


Fig. 10 Dark field image of the nanoscale-NbC in the matrix of the **a** 3.5Si as-welded, **b** 3.5Si-900 weld metal (Red arrows point to NbC of size 5–10 nm, yellow arrows point to NbC of size 10–20 nm)

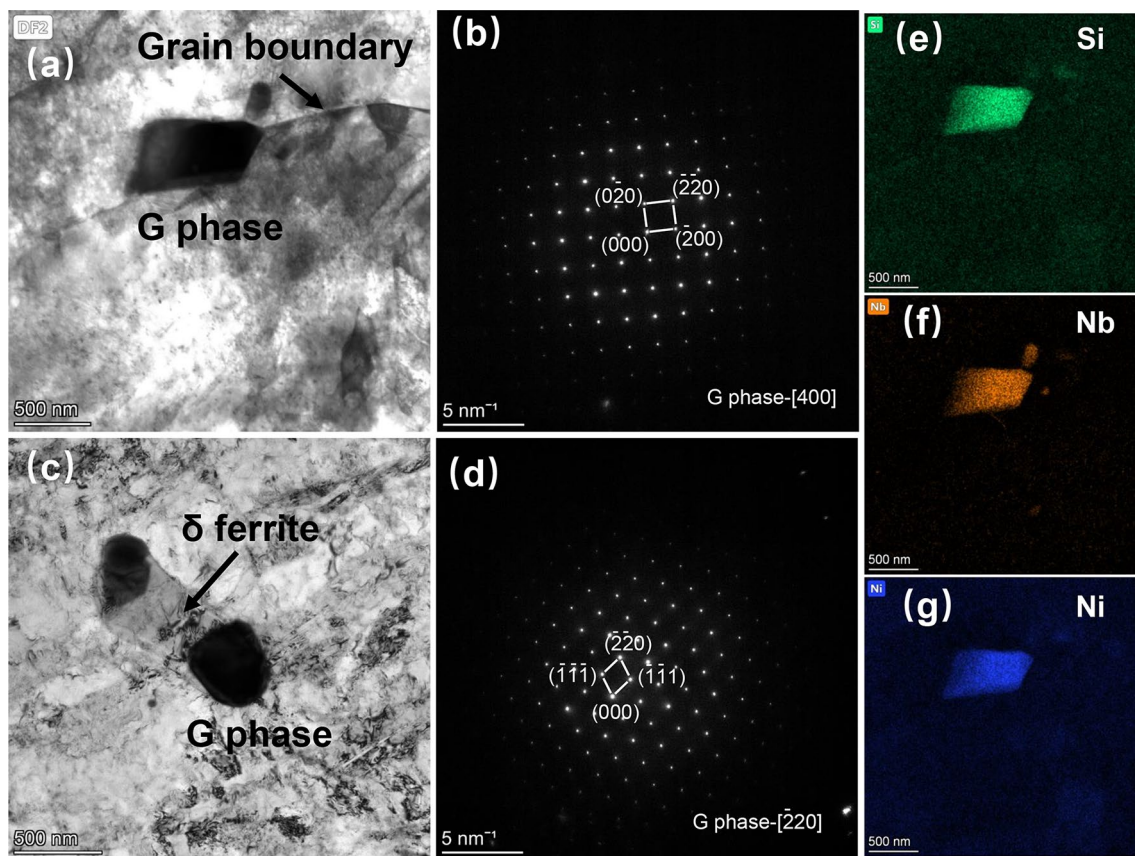


Fig. 11 TEM characterization of G phase: **a** G phase at the grain boundary in 2.5Si-900 weld metal and **b** corresponding SAED pattern, **e**, **f**, **g** corresponding STEM-EDS mappings, **c** G phase at δ/γ interface in 3.5Si-900 and **d** corresponding SAED pattern

transmission electron microscopy (STEM) results, which is consistent with the results of the XRD analysis. Si can promote the formation of the G phase due to its participation in the formation of the G phases and can also promote the transition of NbC to the G phase [27, 28]. G phases tend to nucleate more at grain boundaries [29]. As shown in Fig. 11, in this work, the G phases were formed at the austenite grain boundaries (as shown in Fig. 11a) and the δ/γ interfaces (as shown in Fig. 11c).

3.4 Mechanical Properties

3.4.1 Effect of Martensite on Mechanical Properties

As shown in Fig. 12a, the Vickers hardness of martensite in 2.5Si as-welded weld metal is just 310–320 (HV 0.1), which is slightly higher than the 240–260 (HV 0.1) of austenite in the nearby area, and the martensite content is 3%–4%, which indicates that the strengthening effect of martensite is not obvious for the 2.5Si as-welded weld metal. After SHT, a large amount of martensite formed in the 2.5Si weld metal. As shown in Fig. 12b, the Vickers hardness of martensite in 2.5Si-800 weld metal is 250–270 (HV 0.1), equivalent

to nearby austenite. The decrease in martensite hardness is due to the reduction of C in the matrix, which is also the reason for the martensite transition. As shown in Fig. 13, the surfaces of the tensile fracture of 2.5Si as-welded and 2.5Si-800 weld metal are both dimples, which means that the martensite in 2.5Si-800 weld metal has no significant effect on the tensile fracture behavior. The martensite formed after the SHT has less effect on the strength of the 15Cr–9Ni–Nb weld metal, which is consistent with the results of the tensile test. As shown in Fig. 14a and b, after SHT, the yield strength of 2.5Si weld metal did not rise but declined, and the tensile strength had no significant change.

3.4.2 Effect of Precipitation Behavior on Mechanical Properties

There are two types of precipitations in the as-welded weld metal: the coarse-NbC and nanoscale NbC. As shown in Fig. 15d, the coarse-NbC could be the source of the dimple, promote the dimple nucleation, and reduce the impact toughness. Because NbC was mainly formed at intragranular dislocations and stacking layer dislocations, nanoscale NbC could block dislocation movement and strengthen

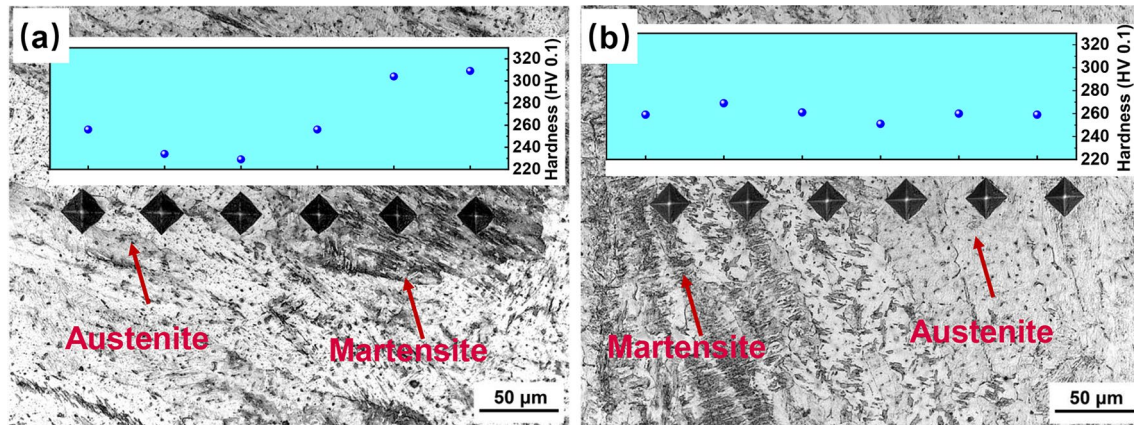


Fig. 12 Vickers microhardness test results: **a** 2.5Si as-welded weld metal, **b** 2.5Si-800 weld metal

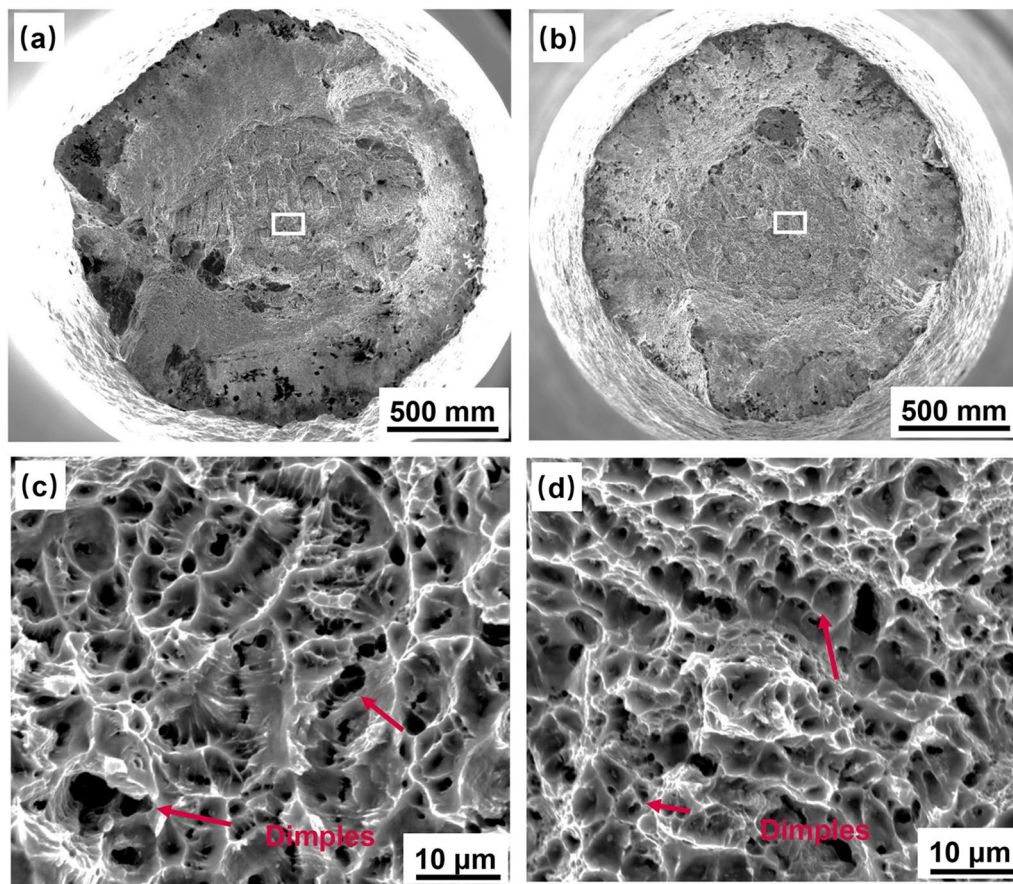


Fig. 13 Surfaces of the tensile fracture of **a, c** 2.5Si as-welded and **b, d** 2.5Si-800 weld metal

the weld metal. During SHT, a large amount of dispersed nanoscale NbC precipitated (as shown in Fig. 10b) and C content in the matrix was reduced. The strengthening effect of the solid solution was weakened due to the decrease of C atoms. Meanwhile, the precipitation strengthening effect was enhanced due to the formation of a large amount of

nanoscale NbC. As shown in Fig. 12a, the yield strength of both 2.5Si and 3.5Si weld metal was declining after SHT, which means that the strengthening effect of the solid solution played a dominant role.

As shown in Fig. 15, the surfaces of the impact fracture of 3.5Si as-welded weld metal were dimples, while there were

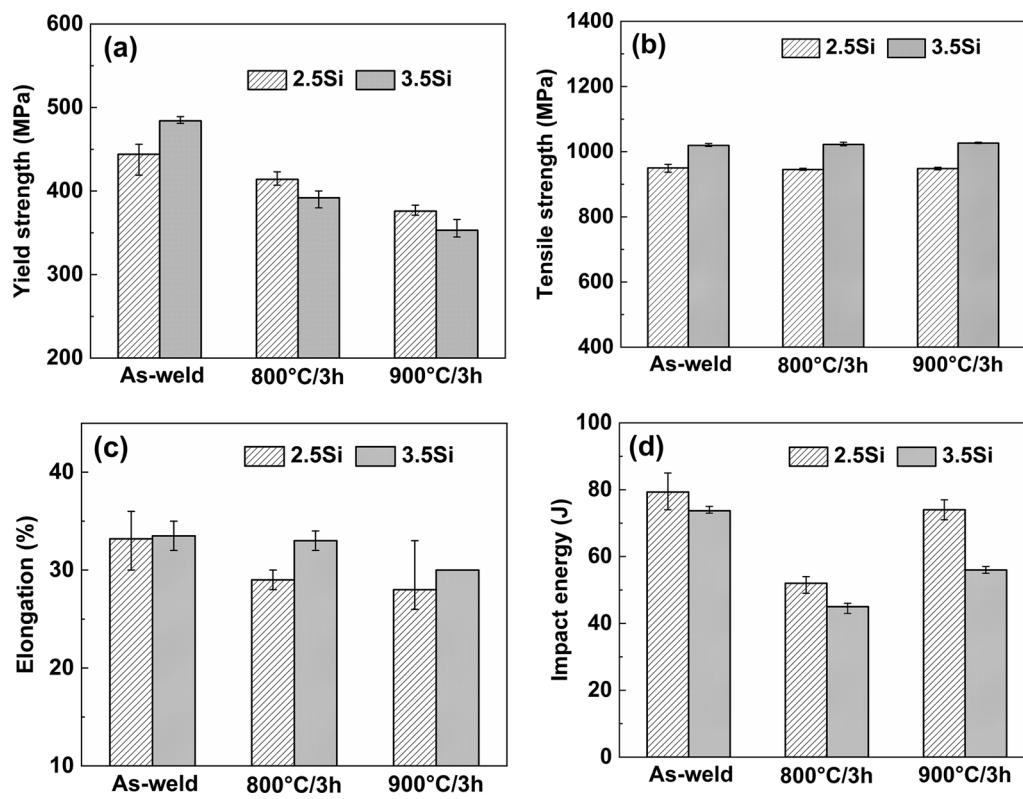


Fig. 14 Changes in room temperature mechanical properties of weld metals: **a** yield strength, **b** tensile strength, **c** elongation, **d** impact energy

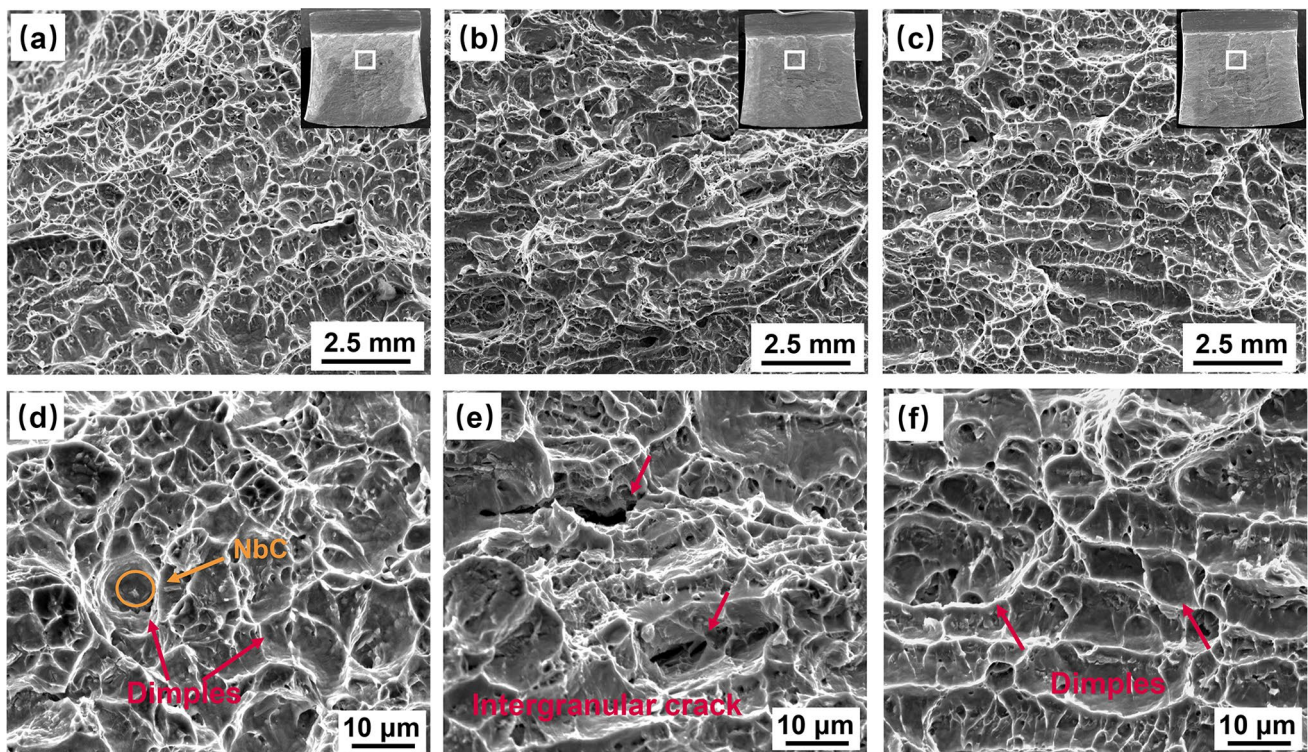


Fig. 15 Surfaces of the impact fracture of **a, d** 3.5Si as-welded, **b, e** 3.5Si-800, **c, f** 3.5-900 weld metal

intergranular cracks on the surfaces of the impact fracture of 3.5Si-800 weld metal. The decline in impact toughness after SHT (as shown in Fig. 14d) was caused by the intergranular fracture. As shown in Fig. 16, the intergranular fracture was caused by the G phase precipitation at the austenite grain boundaries and the δ/γ interfaces. A large amount of G phase formed in the weld metal after SHT, which was located at the austenite grain boundary and the δ/γ interfaces (as shown in Fig. 11). G phase was fragile, and it has been reported in the literature that the G phase was harmful to mechanical properties [30, 31]. Therefore, the formation of a large number of G phases during SHT impaired the impact properties of the weld metal. The impact toughness of 3.5Si weld metal decreased more than 2.5Si weld metal after SHT because of the more G phase formed in the 3.5Si weld metal after SHT due to the elevated Si content.

3.4.3 Effect of $\delta \rightarrow \gamma$ Transition on Mechanical Properties

The δ ferrite in the stainless steel weld metal brings about a second phase strengthening effect, which has already been proved in many studies [32, 33]. The strength of the 3.5Si as-welded weld metal is higher than that of the 2.5Si as-welded weld metal because of the higher δ ferrite content. The $\delta \rightarrow \gamma$ transition occurred during SHT, resulting in lowering δ content in the weld metal, which also reduced the yield strength of the weld metal. The dropped content of δ ferrite due to $\delta \rightarrow \gamma$ transition was higher after 900 °C/3 h treatment than 800 °C/3 h treatment (as shown in Figs. 4 and 6), which led to further degradation of yield strength after 900 °C/3 h (as shown in Fig. 14a). The $\delta \rightarrow \gamma$ transition also resulted in a decrease in the amount of the δ/γ interfaces, as shown in Fig. 6d. After SHT, the G phases formed during SHT, which is located at the austenite grain boundary and the δ/γ interfaces, led to intergranular fracture. This is the main reason for the degradation in impact toughness of 2.5Si and 3.5Si

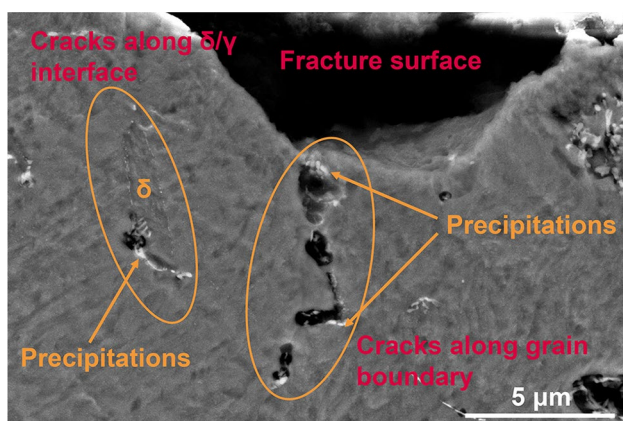


Fig. 16 SEM micrographs of the 3.5Si-800 weld metal impact sample (longitudinal section)

weld metal after 800 °C/3 h. After 900 °C/3 h, the amount of δ/γ interfaces declined significantly because of the $\delta \rightarrow \gamma$ transition, leaving the precipitations on the austenite matrix where the originally δ/γ interfaces were. This type of precipitation promoted dimple formation rather than intergranular crack. The decline of the amount of δ/γ interfaces resulted in the reduction in the intergranular fracture; as a result, the number of dimples increased (as shown in Fig. 15c, f) in the weld metals after 900 °C/3 h. Hence, the impact energy of 2.5Si-900 and 3.5 Si-900 rose compared to 2.5Si-800 and 3.5Si-800, as shown in Fig. 14d.

4 Conclusions

In this work, the microstructure of the as-welded and after-stabilization heat treatments (SHT) weld metal of 15Cr–9Ni–Nb stainless steel was investigated in detail through various characterization methods and the room temperature mechanical properties were also tested. Based on the above investigation, the conclusions can be drawn as follows:

1. In addition to δ ferrite and austenite, a small amount of martensite was formed in the 2.5Si as-welded weld metal, and δ ferrite and austenite were present in the 3.5Si as-welded weld metal. After the SHT, a large amount of martensite was formed in the 2.5Si weld metal because of the decrease of C in the matrix. $\delta \rightarrow \gamma$ transition occurred during the SHT in the weld metals, and transition volume increased with the increase in the SHT temperature.
2. There is a large amount of coarse NbC and few nanoscale NbC in the as-welded weld metal. During the SHT, a large amount of nanoscale NbC formed in the matrix, while a large number of G phases formed at the austenite grain boundaries and the δ/γ interfaces. Because of the higher Si content, there were more G phases formed in the 3.5Si weld metal than 2.5Si weld metal during SHT.
3. The decrease in solid solution C and δ ferrite content led to the decline in yield strength of the weld metal after SHT. The martensite formed in 2.5Si weld metal after SHT had less effect on strength because of the reduction of C. The G phase formed during the SHT reduced the impact energy of the weld metal because it promoted the intergranular fracture, while the $\delta \rightarrow \gamma$ transition reduced the amount of the δ/γ interfaces and avoided the intergranular fracture, which was beneficial for the impact toughness of the weld metals.

Acknowledgements This work was financially supported by the China Institute of Atomic Energy (E141L803J1) and the innovation project of Shenyang National Laboratory for Materials Science (SYNL-2022).

Declarations

Conflict of interest The authors state that there are no conflict of interest to disclose.

References

- [1] J.L. Séran, M.L. Flem, *Structural Materials for Generation IV Nuclear Reactors* (Woodhead Publishing, England, 2017), pp.285–328
- [2] A.L. Johnson, D. Parsons, J. Manzerova, D.L. Perry, K. Dan, B. Hosterman, J.W. Farley, *J. Nucl. Mater.* **328**, 88 (2004)
- [3] C. Schroer, O. Wedemeyer, J. Novotny, A. Skrypnik, J. Konys, *Corros. Sci.* **84**, 113 (2014)
- [4] Y. Kurata, H. Yokota, T. Suzuki, *J. Nucl. Mater.* **424**, 237 (2012)
- [5] V. Tsisar, C. Schroer, O. Wedemeyer, A. Skrypnik, J. Konys, *J. Nucl. Mater.* (2014).
- [6] Y. Kurata, S. Saito, *Mater. Trans.* **50**, 2410 (2009)
- [7] I.G. Vladimir, I.S. Viktor, I.O. Mihail, S.C. Tatyana, *Mater. Sci Power Eng.* **91**, 130 (2015)
- [8] J.C. Lippold, D.J. Kotecki, *Welding Metallurgy and Weldability of Stainless Steels* (Wiley, New Jersey, 2005), pp.140–160
- [9] R.A. Farrar, R.G. Thomas, *J. Mater. Sci.* **18**, 3461 (1983)
- [10] R.A. Farrar, *J. Mater. Sci.* **22**, 363 (1987)
- [11] R.A. Farrar, *J. Mater. Sci.* **20**, 4215 (1985)
- [12] J.J. Smith, R.A. Farrar, *J. Mater. Sci.* **26**, 5025 (1991)
- [13] L. Zhao, S. Wei, D. Gao, S. Lu, *Acta Metall. Sin.-Engl. Lett.* **34**, 11 (2021)
- [14] A.B. Korostelev, S.V. Evropin, A.G. Derzhavin, I.V. Vershinin, A.N. Romanov, *At. Energy* **129**, 1 (2021)
- [15] L. Cinotti, C.F. Smith, H. Sekimoto, L. Mansani, M. Reale, J.J. Sienicki, *J. Nucl. Mater.* **415**, 245 (2011)
- [16] A. Nassour, W.W. Bose, D. Spinelli, *J. Mater. Eng. Perform.* **10**, 693 (2001)
- [17] K. Guan, X. Xu, X. Hong, Z. Wang, *Nucl. Eng. Des.* **235**, 2485 (2005)
- [18] G. Eichelman, F.C. Hull, *Trans. Am. Soc. Met.* **45**, 77 (1953)
- [19] B. Arh, F. Tehovnik, F. Vode, *Metals* **11**, 935 (2021)
- [20] B. Leone, H.W. Kerr, *Weld. J.* **61**, 1 (1982)
- [21] A.F. Padilha, G. Schanz, K. Anderko, *J. Nucl. Mater.* **105**, 77 (1982)
- [22] A.S. Grot, J.E. Spruiell, *Metall. Trans. A* **6**, 2023 (1975)
- [23] J.M. Leitnaker, J. Bentley, *Metall. Trans. A* **8**, 1605 (1977)
- [24] A.R. Jones, P.R. Howell, B. Ralph, *J. Mater. Sci.* **11**, 1600 (1976)
- [25] H. Uno, A. Kimura, T. Misawa, *Sumitomo Search (Japan)* **54**, 48 (1993)
- [26] H.W. Cao, X.H. Luo, G.F. Zhan, S. Liu, *Acta Metall. Sin.-Engl. Lett.* **31**, 81 (2018)
- [27] R.A.P. Ibaez, G. Soares, L. Almeida, I.L. May, *Mater. Charact.* **30**, 243 (1993)
- [28] N. Vaché, P. Steyer, C. Duret-Thual, M. Perez, *Materialia* **9**, 100593 (2020)
- [29] D.J. Powell, R. Pilkington, D.A. Miller, *Acta Metall.* **36**, 713 (1988)
- [30] X.F. Guo, Y.Y. Ni, J.M. Gong, L.Y. Geng, J.Q. Tang, Y. Jiang, X.K. Jia, X.Y. Yang, *Acta Metall. Sin.-Engl. Lett.* **30**, 11 (2017)
- [31] D.M. Knowles, C.W. Thomas, D.J. Keen, Q.Z. Chen, *Int. J. Press. Vessel. Pip.* **81**, 499 (2004)
- [32] D. Hauser, J.E. Vanecho, *Weld J.* **50**, 61 (1982)
- [33] J. Vojvodic-Tuma, B. Sustarsic, F. Vodopivec, *Nucl. Eng. Des.* **238**, 1511 (2008)

Springer Nature or its licensor (e.g. a society or other partner) holds exclusive rights to this article under a publishing agreement with the author(s) or other rightsholder(s); author self-archiving of the accepted manuscript version of this article is solely governed by the terms of such publishing agreement and applicable law.